Computational and Theoretical Chemistry 1006 (2013) 92–99

Contents lists available at SciVerse ScienceDirect

Computational and Theoretical Chemistry

journal homepage: www.elsevier.com/locate/comptc

Pauli potential and Pauli charge from experimental electron density

Vladimir G. Tsirelson [a,*], Adam I. Stash [a,b], Valentin V. Karasiev [c], Shubin Liu [d,*]

[a] Quantum Chemistry Department, Mendeleev University of Chemical Technology, Moscow 125047, Russia
[b] Karpov Institute of Physical Chemistry, Moscow 105064, Russia
[c] Quantum Theory Project, Departments of Physics and of Chemistry, University of Florida, Gainesville, FL 32611, United States
[d] Research Computing Center, University of North Carolina, Chapel Hill, NC 27599-3420, United States

ARTICLE INFO

Article history:
Received 11 July 2012
Received in revised form 18 November 2012
Accepted 20 November 2012
Available online 29 November 2012

Keywords:
Chemical bond
Density functional theory
Electron density

ABSTRACT

In this work, based on the experimental electron density, we present the approximate spatial distributions of the Pauli potential, one of the key quantities in the orbital-free density functional, for three crystalline systems: diamond, cubic boron nitride, and magnesium diboride. Our aim is to reveal a link between the Pauli potential and the orbital-free picture of chemical bond. We also expand the theoretical framework by developing the concept of the Pauli charge density. We find that both these quantities reproduce the electronic shell structure in the atomic core regions, while in the bonding region they reveal the different features for different bonding types, thereby distinguishing between ionic and covalent bond and also identifying the distinction between polar and nonpolar covalent bonds. Therefore, the Pauli potential and its associated charge density can be used as the orbital-free descriptors of chemical bond in the crystalline systems.

1. Introduction

Density functional theory (DFT) has become one of the most powerful tools in computing the electronic structure of molecules and solids [1,2]. It is both theoretically rigorous and computationally efficient. From another side, recent progress in the X-ray diffraction instrumentation [3,4] provides an opportunity for further development of the experimental data treatment methods to become a reliable tool in the detailed study of the physical and chemical properties of solids, which are defined by the electron density. Naturally, these methods are based on density functional theory and usually include quantum-topological analysis of electron density from the bonding point of view [5,6]. However, the most popular implementation of DFT makes use of the Kohn–Sham scheme [7], in which single-particle orbitals are introduced and the *non-interacting* kinetic energy is treated exactly instead of using approximate density functionals [8]. The computational complexity of the Kohn–Sham scheme goes at least as N^3 in a plane wave basis set or N^4 in a localized one, where N is the total number of electrons or basis functions. This relatively high computational cost restricts the extent to which the Kohn–Sham method can be applied to the simulation of large systems of biological and material science relevance. In the recent literature of DFT developments, we have witnessed a renewed surge of efforts to use the density and its derivatives only in the simulation of electronic properties of molecules and crystals. This latter approach is often called orbital-free DFT (OF-DFT), see [9–12] for reviews. The attractiveness of the OF-DFT approach lies in the fact that regardless of the system size, the problem size scales at worst with the volume. However, the difficulty of developing physically valid approximations for the non-interacting kinetic energy density functional has limited the development of effective OF-DFT methods [13–24] severely. The use of orbital-free methods is almost inescapable, however, for the case in which only the electron density reconstructed from X-ray diffraction data is used as the input for analysis of physical and chemical properties. From the viewpoint of developing new approximate orbital-free functionals, the data retrieved from experiments may serve as a reference exactly in the same way as data obtained from the high-level theory.

In the OF-DFT approach, instead of a self-consistent problem for a set of KS orbitals, one obtains a single Euler equation by minimizing the total energy density functional $E[\rho]$ subject to the constraint that the total electron density $\rho(\mathbf{r})$ is normalized to the total number of electrons. The Euler equation has the following Schrödinger-like form [25–27],

$$\{-1/2\nabla^2 + v_\theta(\mathbf{r}) + v_{eff}(\mathbf{r})\}\rho^{1/2}(\mathbf{r}) = \mu\rho^{1/2}(\mathbf{r}), \quad (1)$$

where μ is the chemical potential, $v_\theta(\mathbf{r})$ is the Pauli potential, and $v_{eff}(\mathbf{r})$ is the effective potential. The last quantity is in fact the standard Kohn–Sham potential. It can be decomposed further into the following contributions,

* Corresponding authors. Tel.: +7 499 978 9584; fax: +7 495 609 2964 (V. Tirelson), tel.: +1 919 962 4032; fax: +1 919 962 0417 (S. Liu).
E-mail addresses: vtsirelson@yandex.ru (V.G. Tsirelson), shubin@email.unc.edu (S. Liu).

2210-271X/$ - see front matter © 2012 Elsevier B.V. All rights reserved.
http://dx.doi.org/10.1016/j.comptc.2012.11.015

$$v_{eff}(\mathbf{r}) = v_{es}(\mathbf{r}) + v_{xc}(\mathbf{r}). \quad (2)$$

The electrostatic potential, $v_{es}(\mathbf{r})$, is the sum of the external potential, $v_{ext}(\mathbf{r})$, and the classical inter-electron Columbic repulsion potential, $v_J(\mathbf{r})$,

$$v_{es}(\mathbf{r}) = v_{ext}(\mathbf{r}) + v_J(\mathbf{r}) = -\sum_a \frac{Z_a}{|\mathbf{r}-\mathbf{R}_a|} + \int \frac{\rho(\mathbf{r}')}{|\mathbf{r}-\mathbf{r}'|} d\mathbf{r}'. \quad (3)$$

The exchange–correlation potential, $v_{xc}(\mathbf{r})$, is defined as the functional derivative of the exchange–correlation energy functional $E_{xc}[\rho]$,

$$v_{xc}(\mathbf{r}) = \frac{\delta E_{xc}[\rho]}{\delta \rho}. \quad (4)$$

The term $v_\theta(\mathbf{r})$ in Eq. (1), the Pauli potential [27, 28], stems from the effect of the many-electron wave function anti-symmetry requirement in the kinetic energy [29–31].

Given a system and exchange–correlation functional approximation, the Pauli potential can be obtained readily via the Kohn–Sham orbitals and eigenvalues $\{\varphi_i, \varepsilon_i\}$ as [29]

$$v_\theta(\mathbf{r}) = \sum_{i=1}^{N/2} [\nabla(\varphi_i \rho^{-1/2})^* \cdot \nabla(\varphi_i \rho^{-1/2}) + (\varepsilon_{N/2} - \varepsilon_i) 2\varphi_i^* \varphi_i \rho^{-1}], \quad (5)$$

for the case of N/2 doubly occupied orbitals. The non-negativity of $v_\theta(\mathbf{r})$ is one of the exact properties of the Pauli potential which follows from Eq. (5). At the same time, to the best of our knowledge, no numerical data has been available in the literature for the Pauli potential obtained from the electron density without the use of one-electron orbitals, except for a few atomic and molecular cases [12,22,32]. In this work, we report the first examples of the Pauli potential for a few crystalline systems, namely diamond, cubic boron nitride, and magnesium diboride, approximately reconstructed from experimental (X-ray and synchrotron) electron density measured by accurate diffraction methods. We are also interested in exploring how the chemical bonding features derived from experiment manifest themselves in the Pauli potential in the crystals with different bonding types. Similar studies, for the case of theoretical Kohn–Sham densities, have already been reported for the components of the Kohn–Sham local potentials in atoms [33] and diatomic molecules [34]. In addition, the corresponding charge densities defined through the Poisson equation from the Pauli potential are also presented in this work.

2. Theoretical framework

Conventionally, the total energy density functional $E[\rho]$ can be decomposed into the non-interacting kinetic energy $T_s[\rho]$, the electrostatic energy $E_{es}[\rho]$, and the exchange–correlation energy $E_{xc}[\rho]$,

$$E[\rho] = T_s[\rho] + E_{es}[\rho] + E_{xc}[\rho] \quad (6)$$

where $E_{es}[\rho]$ is the sum of the electron-nuclear attraction $E_{en}[\rho]$, nuclear–nuclear repulsion E_{nn}, and the classical Columbic repulsion $J[\rho]$,

$$E_{es}[\rho] = E_{en}[\rho] + E_{nn} + J[\rho]. \quad (7)$$

The exchange–correlation energy, $E_{xc}[\rho]$, includes the kinetic counterpart of so-called the dynamic electron correlation [35–37]. The foregoing energy decomposition can be re-arranged to separate the Weizsäcker kinetic energy [38]

$$T_W[\rho] = \frac{1}{8}\int \frac{|\nabla\rho(\mathbf{r})|^2}{\rho(\mathbf{r})} d\mathbf{r} = \frac{1}{2}\int |\nabla[\rho^{1/2}(\mathbf{r})]|^2 d\mathbf{r} \quad (8)$$

giving

$$E[\rho] = T_W[\rho] + T_\theta[\rho] + E_{es}[\rho] + E_{xc}[\rho], \quad (9)$$

with the Pauli energy $T_\theta[\rho]$, defined as

$$T_\theta[\rho] \equiv T_s[\rho] - T_W[\rho], \quad (10)$$

where $T_s[\rho]$ is the Kohn–Sham non-interacting kinetic energy functional.

The Pauli potential is defined as the functional derivative of the Pauli energy, $T_\theta[\rho]$, with respect to the electron density:

$$v_\theta(\mathbf{r}) = \frac{\delta T_\theta[\rho]}{\delta\rho} = \frac{\delta T_s[\rho]}{\delta\rho} - \frac{\delta T_W[\rho]}{\delta\rho}. \quad (11)$$

Here the term $\frac{\delta T_W[\rho]}{\delta\rho} = v_W(\mathbf{r})$ is the von Weizsäcker potential (which was recently treated as the steric electronic potential [39]):

$$v_W(\mathbf{r}) = \frac{1}{8}\frac{|\nabla\rho(\mathbf{r})|^2}{\rho^2(\mathbf{r})} - \frac{1}{4}\frac{\nabla^2\rho(\mathbf{r})}{\rho(\mathbf{r})}. \quad (12)$$

Two approaches are available to express the Pauli potential, Eq. (11), explicitly in terms of the electron density and its gradients. One can use an approximate form of either the kinetic energy density functional or the exchange–correlation energy density functional. To obtain the explicit expression for the functional derivative of the non-interacting kinetic energy functional, $\frac{\delta T_s[\rho]}{\delta\rho}$, we can approximate the non-interacting kinetic energy density, $t_s(\mathbf{r})$, in $T_s[\rho] = \int t_s(\mathbf{r})d\mathbf{r}$, within the gradient expansion or conjoint approximations [12]. For example, the Kirzhnits [40] second-order gradient approximation yields

$$t_s(\mathbf{r}) = c_{TF}\rho(\mathbf{r})^{5/3} + \frac{1}{72}\frac{|\nabla(\mathbf{r})|^2}{\rho(\mathbf{r})} + \frac{1}{6}\nabla^2\rho(\mathbf{r}), \quad c_{TF} = \frac{3}{10}(3\pi^2)^{2/3} \quad (13)$$

leading to

$$\frac{\delta T_s[\rho]}{\delta\rho} = \frac{5}{3}c_{TF}\rho(\mathbf{r})^{2/3} + \frac{1}{72}\left\{\frac{|\nabla\rho(\mathbf{r})|^2}{\rho^2(\mathbf{r})} - 2\frac{\nabla^2\rho(\mathbf{r})}{\rho(\mathbf{r})}\right\} = \frac{5}{3}c_{TF}\rho(\mathbf{r})^{2/3} + \frac{1}{9}v_W(\mathbf{r}). \quad (14)$$

As a result, the approximate Pauli potential can be expressed in the form

$$v_\theta(\mathbf{r}) = \frac{5}{3}c_{TF}\rho(\mathbf{r})^{2/3} - \frac{8}{9}v_W(\mathbf{r}). \quad (15)$$

Note that this approach is close to that already exploited by King and Handy [41].

Another way to construct the Pauli potential is to use the Euler Eq. (1) which can be presented in the standard form [42]

$$\frac{\delta T_s[\rho]}{\delta\rho} = \mu - v_{eff}(\mathbf{r}) \quad (16)$$

For a given system, μ = const. The effective potential $v_{eff}(\mathbf{r})$ is defined up to an arbitrary constant, therefore it is convenient to set $\mu = 0$ throughout this work [41]. It is assumed that for finite atomic systems $v_{eff}(\mathbf{r}) \to 0$ with $\mathbf{r} \to \infty$ and $v_\theta(\mathbf{r}) \to 0$ with $\mathbf{r} \to \infty$ [29]. Also the Pauli potential will vanish in the special case of one electron or two electron (singlet) systems.

Taking into account of Eq. (11), we arrive at the following expression for the Pauli potential:

$$v_\theta(\mathbf{r}) = -v_{es}(\mathbf{r}) - v_{xc}(\mathbf{r}) - v_W(\mathbf{r}). \quad (17)$$

This way of computing the Pauli potential, in contrast to Eq. (15), does not involve the use of an approximate kinetic energy functional, but uses an approximate form for the exchange–correlation term. Decomposing the exchange–correlation potential $v_{xc}(\mathbf{r})$ into the exchange, $v_x(\mathbf{r})$, and correlation, $v_c(\mathbf{r})$, parts, $v_{xc}(\mathbf{r}) = v_x(\mathbf{r}) + v_c(\mathbf{r})$, we can calculate it by the known approximate exchange and correlation functional formulas. The simplest one is to use the local

density approximation (LDA) to obtain $v_x(\mathbf{r})$ and $v_c(\mathbf{r})$ potentials. In this work, we employed the von Barth–Hedin exchange and correlation potentials [43].

Eq. (5) can also be used to evaluate the Pauli potential in case that both the density and KS orbitals are given. In that case, if the same approximation is used for the exchange–correlation term, Eq. (5) will produce exactly the same result as Eq. (17) (see Ref. [29] for details).

The Pauli charge density, $q_\theta(\mathbf{r})$, may be defined for potential v_θ by means of the Poisson equation [44–46]

$$\nabla^2 v_\theta(\mathbf{r}) = -4\pi q_\theta(\mathbf{r}). \tag{18}$$

In contrast to the potential v_θ, the associated Pauli charge density $q_\theta(\mathbf{r})$ can be both positive and negative. It also does not depend on an arbitrary constant, such as the case for the constant μ in Eq. (16). It is worth noting that the function $-q_\theta(\mathbf{r}) = \nabla^2 v_\theta(\mathbf{r})$ "works" in the same manner as Laplacian of the electron density. Therefore, this function may be helpful in the topological analysis of the Pauli potential from the bonding viewpoint.

3. Computational details

The Pauli potential in terms of electron density and its derivatives was computed in two different ways: directly using the approximate kinetic energy density within the gradient expansion approximation via Eq. (15), and employing the Euler equation of DFT and the approximate LDA exchange and correlation potentials through Eq. (17). Because the two approximations are of different character, these two approaches are expected to lead to different results. To make a choice by identifying which approximation performs better, we have computed the Pauli potential for the Ne, Ar and Kr atoms, for which accurate numerical data of the Pauli potential are available in the literature [32], using both Eqs. (15) and (17).

The results are shown in Fig. 1. First, we notice that Eq. (15) does not lead to proper behavior of the Pauli potential at small r. The presence of the singular $v_W(\mathbf{r})$ term in Eq. (17) violates the conditions of non-negativity of $v_\theta(\mathbf{r})$ valid for the exact Pauli potential [29,26,47,48]. We found $v_\theta(\mathbf{r}) \leqslant 0$ for r less than 0.033, 0.017 and 0.008 a.u. for Ne, Ar and Kr, respectively. It is certainly far beyond the resolution achievable in present-day X-ray diffraction experiments which are used to reconstruct the electron density in this work. Secondly, the influence of the Laplacian term in $v_W(\mathbf{r})$ is more apparent when the Pauli potential is computed using the gradient expansion approximation of the kinetic energy density in Eq. (15). In this case the values of v_θ are remarkably overestimated at $r < 0.1$ a.u. Thus, the second-order Kirzhnits expansion [40] does not describe properly the kinetic energy density of electrons close to nucleus, where the electron density variations are not small. Inclusion of the higher-order terms does not improve the situation. Further, the Pauli potential, in contrast to the atomic electrostatic potential, which decays monotonically from the nucleus, displays the shell-like structure. The $(n-1)$ humps (potential barriers) in v_θ denote the boundaries between n electronic shells. The outermost hump in v_θ for heavy atoms is almost lost in v_θ computed using Eq. (15). This is one of the reasons why well-behaved approximate forms of $t_S(\mathbf{r})$ are so difficult to find. In contrast, the atomic electronic shell structure is clearly visible when Eq. (17) is used to calculate the Pauli potential. These results convincingly demonstrate that the derivation of the Pauli potential by means of Eq. (17) is preferable in our case. It should also be indicated that our Pauli potentials for the Ne, Ar and Kr atoms computed with (17) using the local von Barth–Hedin exchange and correlation potentials [43] successfully reproduce the peak values, numbers of atomic shells, as well as long range behaviors of v_θ obtained by Nagy [32] using accurate numerical data. Moreover, even quantitative agreement of both sets of the Pauli potentials is observed for these atoms. Therefore our present framework to compute the Pauli potential using Eq. (17) seems to be reliable at least for this limited set of tests. Thus, we follow this approach for the rest of the present work.

The electron density and its derivatives needed for the crystal potential reconstruction were derived from accurate experimental (X-ray and synchrotron) diffraction intensities by means of the structural multipole model [3]. Within it, the atomic core electron densities are modeled by the orbitals of free atoms, while the crystalline valence electron density is presented as the sum of aspherical atomic densities, each of which is expanded into a convergent series over the real combinations of the spherical harmonics up to 4th order, so called multipoles. The core and valence radial densities of multipoles were described by the relativistic orbitals approximated by the exponential functions [49]. The Fourier transforms of the model density, the structure factors, were fitted to the experimental ones by variation of the electronic populations of the multipoles as well as the contraction/expansion parameters of the atomic valence shells. Anisotropic harmonic atomic displacements were accounted for using a standard approach [3]. The reconstructed model (quasi-static) electron density, which was accurate as $\sim$0.005 e bohr^{-3} in the main part of a crystal space (excluding

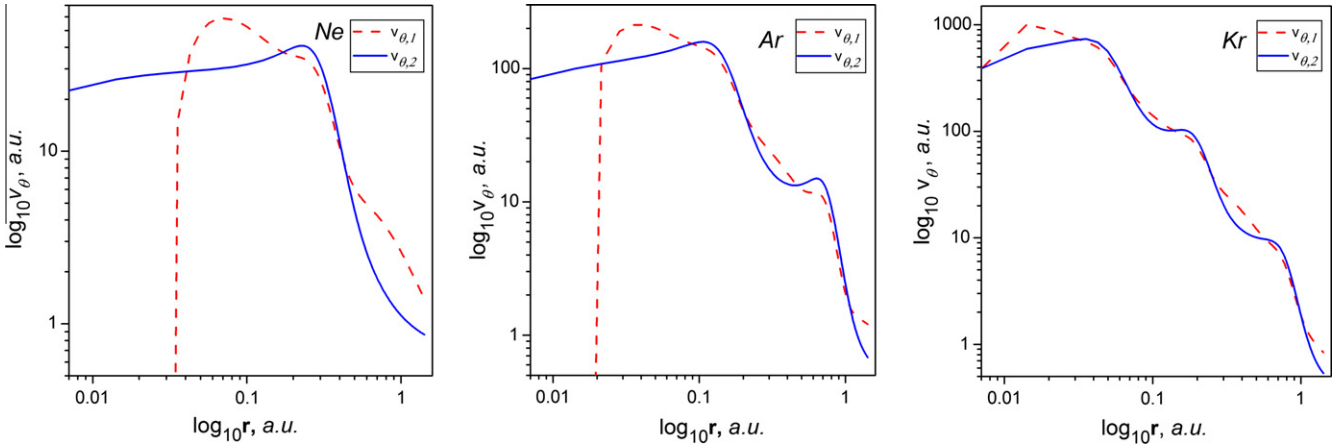

Fig. 1. Pauli potentials computed for Ne, Ar and Kr atoms from relativistic orbitals [49]. Notation: $v_{\theta,1}$ (red dashed curve) stands for the Pauli potential computed using Eq. (15), while $v_{\theta,2}$ (blue solid curve) is computed through Eq. (17). (For interpretation of the references to color in this figure legend, the reader is referred to the web version of this article.)

the regions around the nuclei [50]) was used in the following calculations. For diamond, the multipole-model parameters were derived using synchrotron experimental intensities [51]. The multipole parameters for BN and MgB_2 were taken from our previous works [52,53]. All the results described in this work were obtained using the program WinXPRO [54,55]. We also computed the deformation electron densities for all crystals studied in this work to facilitate the treatment of the potentials and to verify the reliability of our present computational results.

We note that the experimental ground-state electron density is obtained avoiding the variation principle and the self-consistent-field procedure. The experimental and computational electron densities are also derived using the different basis sets. Therefore, there are subtle differences between these densities, which reach ~0.005–0.010 a.u. in the interatomic space (for atoms with $Z < 18$), as is well-documented in the literature [3,4]. An experimental electron density is derived with similar accuracy, as is indicated above. This accuracy is sufficient to compute some density-based properties of molecules and solids with good agreement with independent experimental data [3]. Note that our earlier works [56,57] confirm the feasibility of employing experimental electron densities for approximation of the DFT functionals. Taking into account these facts, we employ the experimental electron density in this work.

4. Results and discussion

The Pauli potential and corresponding charge density for diamond, boron nitride (BN), and MgB_2 crystals are presented in Figs. 2–4, respectively. As shown in Fig. 2a, the Pauli potential $v_\theta(\mathbf{r})$ in diamond peaks on the nuclear positions, decays smoothly and then forms near spherical barriers with a diameter ~0.24 Å around each nucleus. These barriers clearly denote the boundaries between K and L electronic shells of bonded carbon atoms in diamond. Between atomic cores, the Pauli potential diminishes and forms extended near-uniform areas along the nonpolar C–C covalent bond. This reduced Pauli potential reflects the impact of the Pauli exclusion principle on the electronic kinetic energy and promotes electron density accumulation along the C–C bond, as reflected in the deformation electron density [3] (see Fig. 1S in Supplementary material) That the Pauli potential distribution is symmetrical along the C–C bond is a manifestation of the fact that the C–C bond in diamond is nonpolar and covalent. From the $v_\theta(\mathbf{r})$ plot in Fig. 2a, we also can see that the regions of the reduced Pauli potential are slightly compressed by the atomic cores along the C–C line. This however does not influence the near spherical shape of the electron accumulation in the (1 1 0) plane, which is defined by the whole set of bonding mechanisms. The potential $v_\theta(\mathbf{r})$ in the tetrahedral and octahedral crystal holes of diamond also shows the barrier reflecting the symmetry of the atomic positions and separating the zigzag chains of C atoms in the (1 1 0) plane.

These results show how the antisymmetry of the diamond many-electron wave function influences the kinetic energy within atomic cores, promotes formation of regions of reduced Pauli potential around the midpoint of the C–C and contributes to the shape of the tetrahedral and octahedral holes of the potential in the crystal. Compared to the free carbon atom superposition (not shown), we do not observe significant changes in height and position in the Pauli potential barrier that separates the K and L electron shells of bonded carbon atoms. However, the behaviors of the Pauli potential near the nuclei are substantially different. The key feature from the Pauli potential as compared with the free carbon atoms is the extended regions of reduced Pauli potential between atomic cores. These regions with the symmetry axis along the C–C bonds coincide with the regions of electron density accumulation in diamond. These results indicate that the Pauli potential distribution along the C–C bond is a clear indication and manifestation of the homonuclear nonpolar covalent bond.

The associated Pauli charge density, $q_\theta(\mathbf{r})$, Fig. 2b, also shows both the atomic shell structure and the bonding features of bonded atoms in diamond clearly. The charge density $q_\theta(\mathbf{r})$ exhibits positive peaks at the nuclear positions, and alternating regions of depletion and concentration with negatively-valued local maximum of $q_\theta(\mathbf{r})$ at the middle of the C–C covalent bonds. This picture signals that $v_\theta(\mathbf{r})$ is locally depleted in such region ($q_\theta(\mathbf{r}) < 0$). Simultaneously, the local concentration of the Pauli potential ($q_\theta(\mathbf{r}) > 0$) is observed in the crystal holes. Note that positive areas of $q_\theta(\mathbf{r})$ around atomic cores coincide with maxima in $v_\theta(\mathbf{r})$.

Put together, these results demonstrate that the three-dimensional distributions of the Pauli potential and corresponding charge density provide orbital-free information about both the atomic

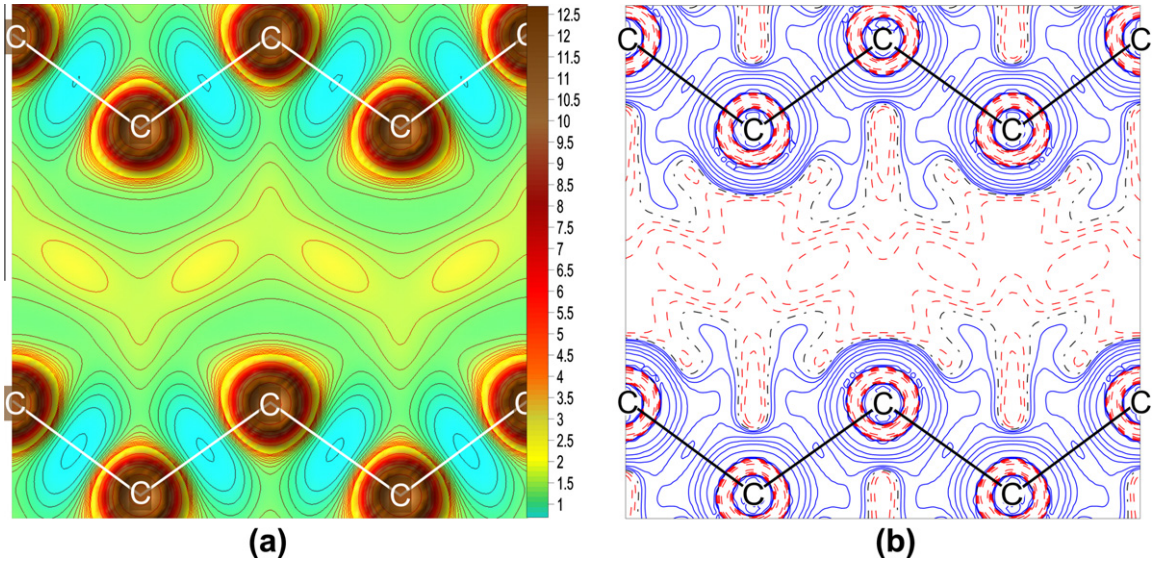

Fig. 2. The Pauli potential (a) and its associated charge density (b) for diamond in the (1 1 0) plane. Here and below the red curves correspond to positive values of the charge densities, while the blue curves denote the negative values. Line intervals are 0.1 a.u. for Pauli potential and ±2, 4, 8×10^n ($-2 < n < 3$) a.u. for charge density. (For interpretation of the references to color in this figure legend, the reader is referred to the web version of this article.)

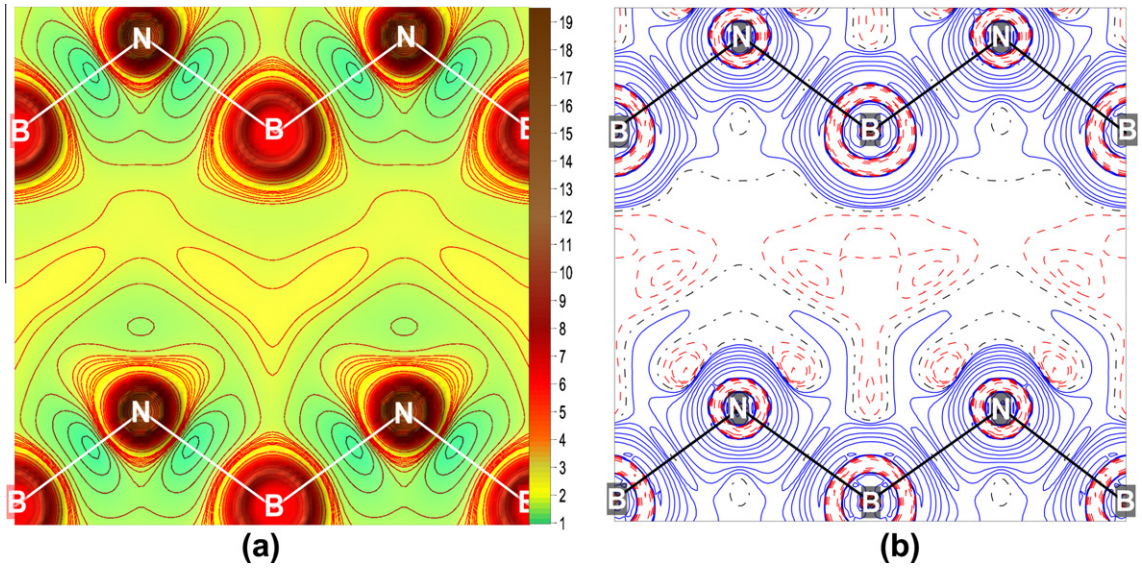

Fig. 3. The Pauli potential (a) and its associated charge density (b) for boron nitride, BN, plane (110). Contour intervals are 0.1 a.u. for the Pauli potential and ±2, 4, 8 × 10^n ($-2 < n < 3$) a.u. for the charge density.

inner shell structure and the nonpolar covalent bonding features at least for this crystalline system.

Fig. 3 shows the results for the boron nitride crystal with the cubic sphalerite structure. The Pauli potential in BN also peaks at the nuclear positions and displays potential barriers between K and L electronic shells of both atoms. However, in contrast to diamond, the asymmetrical nature of the surroundings causes the shape of these barriers to be non-spherical and the barrier is twice as high for the N atom as compared with B atom. The distance from the barrier maximum to the boron position is 0.33 Å and that to the nitrogen position is ≈0.20 Å (Fig. 3a), both of which are very close to those in the free atoms. Between atomic cores, the Pauli potential gradually diminishes from B towards N and reaches a minimum at the point 0.98 Å away from the B atom. This minimum of $v_\theta(\mathbf{r})$ on the B–N bonds is well localized and shifted towards the N atom, which is more electronegative and tends to attract electrons more strongly to its side. Thus, the $v_\theta(\mathbf{r})$ minimum position on the B–N bond line reflects the difference in the electronegativities of atoms involved in this bond. It is interesting to note that the electrostatic potential does not show strong asymmetry along B–N. Therefore electrostatic interaction is not a dominating factor governing this shift, which results from the combined effect of three contributions, $v_{es}(\mathbf{r})$, $v_{xc}(\mathbf{r})$ and $v_W(\mathbf{r})$ see Eq. (17). The aforementioned minima exhibit the tetrahedral arrangement at the N atom position linked by potential bridges to each other. We also note that the potential near the N atoms decays slowly along the continuation of the B–N bond towards the crystal holes. In diamond such a feature is not observed. As in diamond, the potential $v_\theta(\mathbf{r})$ in the tetrahedral and octahedral crystal holes in BN separates the zigzag chains of atoms in the (1 1 0) plane. It is nearly flat and higher than that in the interatomic regions.

These results indicate that the contribution to the kinetic energy from the Pauli exclusion principle manifests itself in solid cubic BN by distorting the shape of atomic cores, shifting the $v_\theta(\mathbf{r})$ minima along the B–N bonds towards the N atoms, and enhancing the $v_\theta(\mathbf{r})$ potential in the tetrahedral and octahedral crystal holes. The regions of reduced Pauli potential along B–N lines coincide with regions of electron density accumulation during the formation of the B–N bond, similar to what we found in diamond. Thus, this feature of the Pauli potential reflects the formation of the heteronuclear polar covalent B–N bond.

The Pauli charge density distribution, $q_\theta(\mathbf{r})$, Fig. 3b, provides equivalent information about the shell electronic structure and bonding features for the solid BN crystal. It exhibits a negative region near the center of the B–N bond with a slight decrease toward the N atom which corresponds the more electronegative nature of N than B. Note that positive regions of $q_\theta(\mathbf{r})$ coincide with maxima in $v_\theta(\mathbf{r})$, as seen in diamond. The Pauli charge density near the atomic cores is unreliable because of distortions in the experimental electron density close to nuclei [3].

These results again demonstrate that Pauli potential and associated charge density are able to reproduce the atomic shell structures and display the polar-covalent nature of the B–N bond in solid BN.

The structure of the magnesium diboride crystalline, MgB_2, with space group of *P*6/*mmm*, is formed by a hexagonal packed monolayer of Mg atoms separated by graphite-like networks of boron atoms (see Fig. 2S in Supplementary material). This homonuclear nonpolar B–B covalent bond, however, is different from that in diamond because of its electron deficient nature. As reported in [53], the B–B interactions in the boron layer exhibit strong σ- and π-bonding components, while along the *c* direction the layers are linked by the weak closed-shell B–B interactions, which can be assigned to interlayer dispersion interactions. The Mg–B closed-shell interactions are typical ionic bonds, accompanied by a charge transfer of about 1.5(1) electrons from Mg atoms to the boron network [53]. Thus, distinct from both diamond and boron nitride crystals, this system includes two different categories of chemical bonds as defined by criteria of the Quantum Theory of Atoms in Molecules and Crystals [5]. They are ionic (Mg–B) and electron deficient covalent (B–B) bonds. No Mg–Mg interactions were identified in MgB_2 [53].

Fig. 4 shows the Pauli potential and Pauli charge distributions for this crystal in three different planes to expose the different kinds of chemical interactions within the crystal. From Fig. 4a and b, we can see that in the hexagonal-packed monolayer of Mg atoms both the Pauli potential and Pauli charge distributions are markedly different from those for the covalently bonded systems. The outermost electronic shell of Mg forms near-uniform, rather symmetrical, and relatively low potential regions in the basal plane (Fig. 4a) as well as along the *c* axis of the unit cell. The Mg–Mg distances are 3.520 Å along the *c* axis and 3.085 Å in the basal plane.

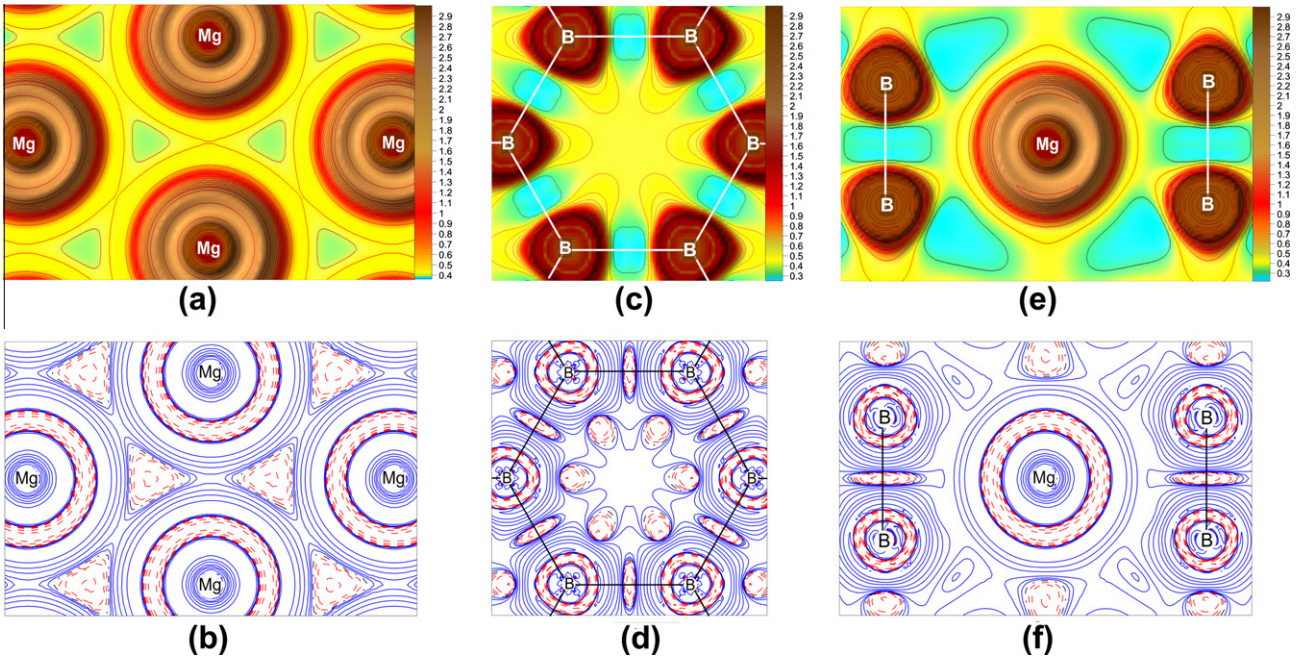

Fig. 4. The Pauli potential (a, c and e) and its associated charge density (b, d and f) for magnesium diboride, MgB_2. Sections in a and b go through the Mg atoms in the basal plane of the crystal unit cell, planes in c and d go through the boron atom network. The "inclined" sections e and f show the ionic Mg–B bonds. Contour intervals are 0.2 (a) and 0.1 (c and e) a.u. for the Pauli potential and $\pm 2, 4, 8 \times 10^n$ $(-2 < n < 3)$ a.u. for the charge density.

The latter value is less twice the metallic radius of Mg, 3.2 Å. However, the geometrical difference does not lead to formation of the restricted plateau in the Pauli potential between Mg atoms, such as is observed in diamond and BN: the Pauli potential along Mg–Mg lines resemble each other. In these areas the Pauli charge density displays a complicated character, highlighted by regions of the Pauli potential depletion and concentration forming space-restricted regions. Thus, although the crystal chemistry geometrical criteria allow the existence a metallic bond in the basal plane of MgB_2, we do not identify such Mg–Mg interactions in terms of the Pauli potential.

For the graphite-like monolayer of boron atoms, along the B–B bond (Fig. 4c), the Pauli potential barrier maximum separating the K and L electronic shells is placed at 0.33 Å from the B nucleus position. This barrier slowly decays in the non-bonding directions (one of them coincides with continuation of the B–B bond), while between atomic cores the Pauli potential is practically uniform over the space volume spanning the B–B covalent bond. Also, the potential $v_\theta(\mathbf{r})$ has a flat extension in the direction perpendicular to the boron network at the B–B midpoint (Fig. 5). This feature may be related to the existence of a weak closed-shell B–B interaction between the boron layers.

The Pauli charge density along the B–B bond (Fig. 4f), is different from that of the covalent and polar covalent bonds in diamond and BN. There exists a small potential concentration region around the midpoint of the B–B bond, which is confined within the near-spherical regions with $q_\theta(\mathbf{r}) < 0$. We can speculate that this charge accumulation can serve as a criterion to distinguish electron deficient covalent bonds from regular covalent bonds. This supposition demands further checks on other systems however.

Along each of B–Mg bonds, as shown in Fig. 4e, $v_\theta(\mathbf{r})$ exhibits a barrier at a distance of 0.35 Å from the B atom. Further, the Pauli potential has a double-humped form separating K, L and M electronic shells of Mg atom with the outermost barrier situated at 0.72 Å from the Mg. Beyond the L electronic shell of Mg, the Pauli potential forms near-spherical equipotential region spanning the Mg atom core. No clear potential minima on the B–Mg bonds, similar to those in BN, were found. This behavior may be understood in the context of the small directionality of twelve ionic Mg–B bonds in a crystal [53]. The pattern shown for the Mg–B ionic bond is different from both the homonuclear and polar covalent bonds.

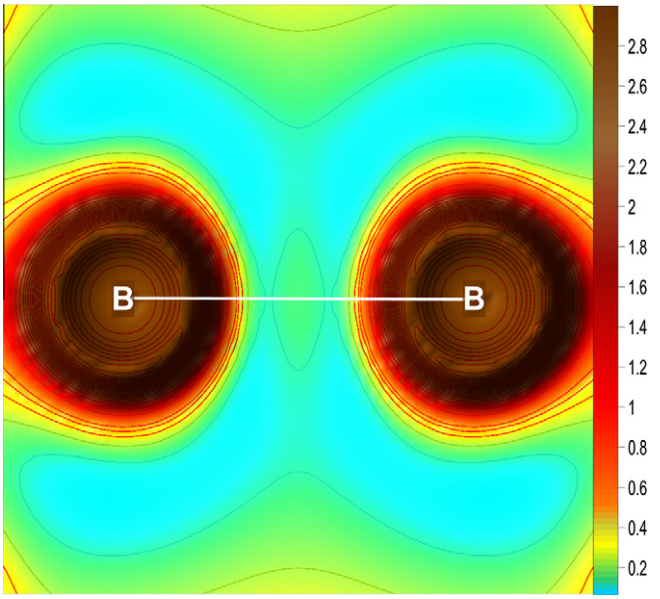

Fig. 5. MgB_2: The Pauli potential in the plane which is going perpendicular to the boron network and includes the B–B bond. Contour interval is 0.1 a.u.

Put together, the results from the three different kinds of crystals, diamond, BN, and MgB_2, provide the first collection of accurate numerical data for the Pauli potential and Pauli charge density. They yield a general view of their three-dimensional behavior for different bonding systems with ionic, polar and nonpolar covalent, and electron-deficient covalent interactions.

Besides providing insights about the local behaviors of the Pauli potential and charge in crystals, the present results can be useful in

at least the following two ways. First, any of these quantities can be utilized as reliable descriptors or indicators of the bonding nature of a system which are not based on orbital representations. From Figs. 2–4, we found that these quantities behave substantially differently in the bonding region with respect to different bonding interaction types. They can distinguish not only between ionic and covalent bonds, but also identify the differences from polar to nonpolar bonds. Second, our results derived from the accurate experimental electron density provide useful reference data for the development of better-behaved and more accurate approximations for the Pauli potential in OF-DFT. What we have observed in this work partly explains why an approximate kinetic energy density functional is so difficult to find, because in the corresponding Pauli potential distribution the information about both atomic shell structure and bonding characteristics is required.

5. Conclusions

The Pauli potential is one of key quantities in orbital-free density functional theory. Its local behavior is still not well understood except for a few simple systems. In this work use of the experimental electron density, allows us, for the first time, to present numerical three-dimensional distribution data for the Pauli potential and its associated Pauli charge density for three crystalline systems, diamond, boron nitride, and magnesium diboride, with different bonding types including ionic, nonpolar covalent, and polar covalent interactions. An important finding is that these quantities reproduce the electronic shell structure of solids. They also are able to reveal bonding-specific features for various bonding types. They distinguish between ionic and covalent bonds and also identify the difference between polar and nonpolar bonds. Thus, these quantities can be used immediately to characterize chemical bonding in molecular and crystalline systems in terms of the potentials, i.e. they can be used as orbital-free descriptors of chemical bonding.

Acknowledgements

We acknowledge informative conversations with Professor Sam Trickey with thanks. VGT and AIS thank the Russian Foundation for Basic Research for financial support, Grant 10-03-00611-a. This work was also supported by Russian Ministry for Education and Science. VVK was supported by the U.S. Dept. of Energy under TMS Grant DE-SC0002139. We acknowledge the use of the computational resources provided by the Research Computing Center at University of North Carolina at Chapel Hill.

Appendix A. Supplementary material

Supplementary data associated with this article can be found, in the online version, at http://dx.doi.org/10.1016/j.comptc.2012.11.015.

References

[1] R.G. Parr, W. Yang, Density Functional Theory of Atoms and Molecules, Oxford University Press, Oxford, 1989.
[2] R.M. Dreizler, E.K.U. Gross, Density Functional Theory: An Approach to the Quantum Many-Body Problem, Springer-Verlag, New York, 1990.
[3] V.G. Tsirelson, R.P. Ozerov, Electron Density and Bonding in Crystals, Inst. Physics Publ., Bristol and Philadelphia, 1996.
[4] C. Gatti, P. Macchi, Modern Charge-Density Analysis, Springer, Dordrecht Heidelberg, London, New York, 2012.
[5] R.F.W. Bader, Atoms in Molecules: A Quantum Theory, Oxford University Press, New York, 1990.
[6] C. Matta, R. Boyd, The Quantum Theory of Atoms in Molecules: From Solid State to DNA and Drug Design, Wiley-VCH, Weinheim, 2007.
[7] W. Kohn, L.J. Sham, Self-consistent equations including exchange and correlation effects, Phys. Rev. 140 (1965) A1133–A1138.
[8] P. Hohenberg, W. Kohn, Inhomogeneous electron gas, Phys. Rev. B136 (1964) 864–871.
[9] H. Chen, A. Zhou, Orbital-free density functional theory for molecular structure calculations, Numer. Math. Theor. Meth. Appl. 1 (2008) 1–28.
[10] Y.A. Wang, E.A. Carter, Orbital-free kinetic energy density functional theory, in: S.D. Schwartz (Ed.), Theoretical Methods in Condensed Phase Chemistry, Kluwer, Dordrecht, 2000, pp. 117–174.
[11] V.L. Ligneres, E. Carter, An Introduction to Orbital-Free Density Functional Theory, in: S. Yip (Ed.), Handbook of Materials Modeling, Springer, Dordrecht, Berlin, Heidelberg, New York, 2005, pp. 137–148.
[12] V.V. Karasiev, R.S. Jones, S.B. Trickey, F.E. Harris, Recent advances in developing orbital-free kinetic energy functionals, in: J.L. Paz, A.J. Hernandez (Eds.), New Developments in Quantum Chemistry, Research Signposts, Kerala, 2009, pp. 25–54.
[13] G. Senatore, K.R. Subbaswamy, Density dependence of the dielectric constant of rare gas crystals, Phys. Rev. B34 (1986) 5754–5759.
[14] T.A. Wesolowski, A. Warshel, Frozen density functional approach for ab-initio calculations of solvated molecules, J. Phys. Chem. 97 (1993) 8050–8053.
[15] O. Roncero, M.P. de Lara-Castells, P. Villarreal, F. Flores, J. Ortega, M. Paniagua, A. Aguado, An inversion technique for the calculation of embedding potentials, J. Chem. Phys. 129 (2008) 184104.
[16] S. Fux, C.R. Jacob, J. Nugebauer, L. Visscher, M. Reiher, Accurate frozen-density embedding potentials as a first step towards a subsystem description of covalent bonds, J. Chem. Phys. 132 (2010) 164101.
[17] J.D. Goodpaster, N. Ananth, F.R. Manby, T.F. Miller III, Exact nonadditive kinetic potentials for embedded density functional theory, J. Chem. Phys. 133 (2010) 084103.
[18] A.S. Iyengar, M. Ernzerhof, S.N. Maximov, G.E. Scuseria, Challenge of creating accurate and effective kinetic energy functionals, Phys. Rev. A63 (2001) 052508.
[19] N. Choly, E. Kaxiras, Kinetic energy density functionals for non-periodic systems, Solid State Commun. 121 (2002) 281.
[20] F. Tran, T.A. Wesolowski, Link between the kinetic- and exchange-energy functionals in the generalized gradient approximation, Int. J. Quant. Chem. 89 (2002) 441–446.
[21] V.V. Karasiev, S.B. Trickey, F.E. Harris, Born-oppenheimer interatomic forces from simple, local kinetic energy density functionals, J. Compos. – Aided Mater. Des. 13 (2006) 111–129.
[22] V.V. Karasiev, R.S. Jones, S.B. Trickey, F.E. Harris, Constraint-based single-point approximate kinetic energy functionals, Phys. Rev. B80 (2009) 245120.
[23] V.V. Karasiev, S.B. Trickey, Issues and challenges in orbital-free density functional calculations, Comput. Phys. Commun. 183 (2012) 2519–2527.
[24] S.B. Trickey, V.V. Karasiev, R.S. Jones, Conditions on the Kohn–Sham kinetic energy and associated density, Int. J. Quant. Chem. 109 (2009) 2943–2952.
[25] B.M. Deb, S.K. Ghosh, New method for the direct calculation of electron density in many-electron systems. I. Application to closed-shell atoms, Int. J. Quantum Chem. 23 (1983) 1–26.
[26] M. Levy, J.P. Perdew, V. Sahni, Exact differential equation for the density of a many-particle system, Phys. Rev. A30 (1984) 2745–2748.
[27] N.H. March, The local potential determining the square root of the ground-state electron density of atoms and molecules from the Schrödinger equation, Phys. Lett. 113A (1986) 476–478.
[28] N.H. March, The density amplitude ρ½ and the potential which generates it, J. Comput. Chem. 8 (1987) 375–379.
[29] M. Levy, H. Ou-Yang, Exact properties of the Pauli potential, Phys. Rev. A38 (1988) 625–629.
[30] C. Herring, M. Chopra, Some tests of an approximate density functional for the ground-state kinetic energy of a fermion system, Phys. Rev. A37 (1988) 31–42.
[31] A. Holas, N.H. March, Construction of the Pauli potential, Pauli energy, and effective potential from the electron density, Phys. Rev. A44 (1991) 5521–5536.
[32] A. Nagy, Analysis of Pauli potential in atoms and ions, Acta Phys. Hung. 70 (1991) 321–331.
[33] O. Gritsenko, R. van Leeuwen, E.J. Baerends, Analysis of electron interaction and atomic shell structure in terms of local potentials, J. Chem. Phys. 101 (1994) 8955–8964.
[34] E.J. Baerends, O. Gritsenko, A Quantum chemical view of density functional theory, J. Phys. Chem. A101 (1997) 5383–5403.
[35] M. Levy, J.P. Perdew, Hellmann–Feynman, virial, and scaling requisites for the exact universal density functionals. Shape of the correlation potential and diamagnetic susceptibility for atoms, Phys. Rev. A32 (1985) 2010–2021.
[36] S.B. Liu, R.G. Parr, Expansions of the correlation-energy density functional Ec[ρ] and its kinetic-energy component Tc[ρ] in terms of homogeneous functionals, Phys. Rev. A53 (1996) 2211–2219.
[37] S.B. Liu, R.C. Morrison, R.G. Parr, Approximate scaling properties of the density functional theory Tc for atoms, J. Chem. Phys. 125 (2006) 174109.
[38] C.F. von Weizsäcker, Zur Theorie der Kernmassen, Z. Phys. 96 (1935) 431–444.
[39] S.B. Liu, On the relationship between densities of Shannon entropy and Fisher information for atoms and molecules, J. Chem. Phys. 126 (2007) 244103.
[40] D.A. Kirzhnits, Quantum corrections to the Thomas–Fermi equation, Sov. Phys. JETP 5 (1957) 64–72.
[41] R.A. King, N.C. Handy, Kinetic energy functionals from the Kohn–Sham potential, Phys. Chem. Chem. Phys. 2 (2000) 5049–5056.
[42] S.B. Liu, P.W. Ayers, Functional derivative of noninteracting kinetic energy density functional, Phys. Rev. A70 (2004) 022501.

[43] U. von Barth, L. Hedin, A local exchange–correlation potential for the spin polarized case. I, C: Solid State Phys. 5 (1972) 1629–1642.
[44] S.B. Liu, P.W. Ayers, R.G. Parr, Alternative definition of exchange–correlation charge in density functional theory, J. Chem. Phys. 111 (1999) 6197–6203.
[45] A. Goerling, New KS method for molecules based on an exchange charge density generating the exact local KS exchange potential, Phys. Rev. Lett. 83 (1999) 5459–5462.
[46] G. Menconi, D.J. Tozer, S. Liu, Atomic and molecular exchange–correlation charges in Kohn–Sham theory, Phys. Chem. Chem. Phys. 2 (2000) 3739–3742.
[47] C. Herring, Explicit estimation of ground-state kinetic energies from electron densities, Phys. Rev. A34 (1986) 2614–2631.
[48] N.H. March, Concept of the Pauli potential in density functional theory, J. Molec. Structure – THEOCHEM 943 (2010) 77–82.
[49] P. Macchi, P. Coppens, Relativistic analytical wavefunctions and scattering factors for neutral atoms beyond Kr and for All chemically important ions up to I^-, Acta Cryst. A57 (2001) 656–662.
[50] V.G. Tsirelson, The mapping of electronic energy distributions using experimental electron density, Acta Cryst. B58 (2002) 632–639.
[51] H. Svendsen, J. Overgaard, R. Busselez, B. Arnaud, P. Rabiller, A. Kurita, E. Nishibori, M. Sakata, M. Takata, B.B. Iversen, Multipole electron-density modelling of synchrotron powder diffraction data: the case of diamond, Acta Cryst. A66 (2010) 458–469.
[52] V.G. Tsirelson, A.I. Stash, S. Liu, Quantifying steric effect with experimental electron density, J. Chem. Phys. 133 (2010) 114110.
[53] V. Tsirelson, A. Stash, M. Kohout, H. Rosner, H. Mori, S. Sato, S. Lee, A. Yamamoto, S. Tajima, Yu. Grin, Features of the electron density of magnesium diboride reconstructed from accurate X-ray diffraction data, Acta Cryst. B59 (2003) 575–583.
[54] A. Stash, V. Tsirelson, WinXPRO: a program for calculating crystal and molecular properties using multipole parameters of the electron density, J. Appl. Cryst. 35 (2002) 371–373.
[55] A.I. Stash, V.G. Tsirelson, Modern opportunities of calculating physical properties of crystals using experimental electron density, Cryst. Report 50 (2005) 209–216.
[56] V. Tsirelson, A. Stash, On functions and quantities derived from the experimental electron density, Acta Cryst. A60 (2004) 418–426.
[57] V.G. Tsirelson, Interpretation of experimental electron densities by combination of the QTAMC and DFT, in: C. Matta, R. Boyd (Eds.), The Quantum Theory of Atoms in Molecules: From Solid State to DNA and Drug Design, Wiley-VCH, Weinheim, 2007, pp. 259–283.